

# Electric Field Control of the Verwey Transition and Induced Magnetoelectric Effect in Magnetite

Jared J. I. Wong, Adrian G. Swartz, Renjing Zheng, Wei Han, and Roland K. Kawakami\*

*Department of Physics and Astronomy, University of California, Riverside, CA 92521, USA*

(Dated: November 20, 2021)

We incorporate single crystal  $\text{Fe}_3\text{O}_4$  thin films into a gated device structure and demonstrate the ability to control the Verwey transition with static electric fields. The Verwey transition temperature ( $T_V$ ) increases for both polarities of the electric field, indicating the effect is not driven by changes in carrier concentration. Energetics of induced electric polarization and/or strain within the  $\text{Fe}_3\text{O}_4$  film provide a possible explanation for this behavior. Electric field control of the Verwey transition leads directly to a large magnetoelectric effect with coefficient of 585 pT m/V.

PACS numbers: 75.47.Lx, 71.27.+a, 75.85.+t, 71.30.+h

Electric field control of magnetic and metal-to-insulator transitions in highly correlated materials has generated great interest both scientifically and technologically [1–5]. Magnetite ( $\text{Fe}_3\text{O}_4$ ) is a highly correlated material that undergoes the well-known Verwey transition with sharp changes in the electric, magnetic, and structural properties [6–8]. Following over seven decades of intense research since its discovery in 1939, the origin of the Verwey transition as a charge order-disorder transition has become clear experimentally just in the last few years [9–15]. In this Letter, we report the surprising observation of electric field control of the Verwey transition in  $\text{Fe}_3\text{O}_4$  thin films. An electric field applied by electrostatic gates is found to stabilize the Verwey structure and increase the transition temperature ( $T_V$ ). Furthermore, electrical control of  $T_V$  leads to a new mechanism for generating a magnetoelectric effect. We obtain a magnetoelectric coefficient of 585 pT m/V, which is one of the largest for a single-phase material. These results provide an alternative approach to advanced electronics, information processing, and spintronics [16–19].

Magnetite is the oldest known magnetic material (lodestone) and the Verwey transition at  $T_V \sim 120$  K is one of the first examples of a metal-to-insulator transition in which the insulating phase is generated by electron-electron correlations [6–8]. The Verwey transition also includes sharp changes to the structure and magnetization [8]. Cooling through  $T_V$ , the unit cell structure changes from inverse-spinel to monoclinic and the magnetization exhibits a sharp decrease below  $T_V$  [8]. This coupling between the electronic, magnetic, and structural properties makes magnetite very attractive for exploring tuning of magnetoelectric behavior in correlated materials which could lead to novel functionality.

Previous demonstrations of electric field control of magnetic and metal-to-insulator transitions have resulted from various effects including current-induced breakdown of the insulating state [2, 3, 20], field-induced changes of carrier concentration [4, 21], field-induced strain generated by growth on piezoelectric substrate (i.e. composite system) [5, 22–24]. The effect reported here is distinct

from these previous categories. Unlike current-induced breakdown which is a highly non-equilibrium process, the present effect produces a true change in the equilibrium phase transition. We also find that this effect is not due to changes in carrier concentration, as shown by a symmetric dependence of  $T_V$  on gate voltage. Finally, this effect does not rely on external strain provided by adjacent layers. Thus, the electric field control of the Verwey transition represents a new type of electric field control in a highly correlated material.

$\text{Fe}_3\text{O}_4$  films of 50 nm thickness are grown on double-side polished MgO(001) substrates using reactive molecular beam epitaxy (MBE) in ultrahigh vacuum (UHV) with a base pressure of  $1 \times 10^{-10}$  torr. MgO substrates are first rinsed with de-ionized (DI) water. After loading into the MBE chamber, substrates are annealed at 600°C for 45 minutes. A 10 nm MgO buffer layer is grown at 350°C via electron beam (e-beam) deposition from an MgO source [25]. Next, the  $\text{Fe}_3\text{O}_4$  layer is grown at 200°C by depositing elemental Fe in a molecular oxygen partial pressure of  $1.2 \times 10^{-7}$  torr. The Fe is evaporated from a thermal effusion cell at a rate of  $\sim 0.13$  nm/min (for pure Fe). The single-crystal structure is verified through *in situ* reflection high energy electron diffraction (RHEED) and low energy electron diffraction (LEED), as shown in Figs. 1a, 1b, and 1c inset.  $\theta - 2\theta$  high resolution x-ray diffraction (HRXRD) scans exhibit a  $\text{Fe}_3\text{O}_4(004)$  peak near the MgO(002) substrate peak (Fig. 1c). Kiessig interference fringes indicate atomically smooth interfaces and verify the film thickness.

Electrical properties of  $\text{Fe}_3\text{O}_4$  films are characterized using standard dc four-point probe measurements (Figure 1d inset). Resistance values are obtained from current-voltage ( $I$ - $V$ ) curves, which exhibit linear dependence (Figure 1e) above 70 K. The temperature dependence of resistance (Figure 1d, blue) exhibits a metal-to-insulator transition with a substantially higher resistance below 117 K, indicating the Verwey transition. Temperature dependence curves are measured as a function of increasing temperature, with the temperature stabilized for 10 min before a measurement is taken. For each tem-

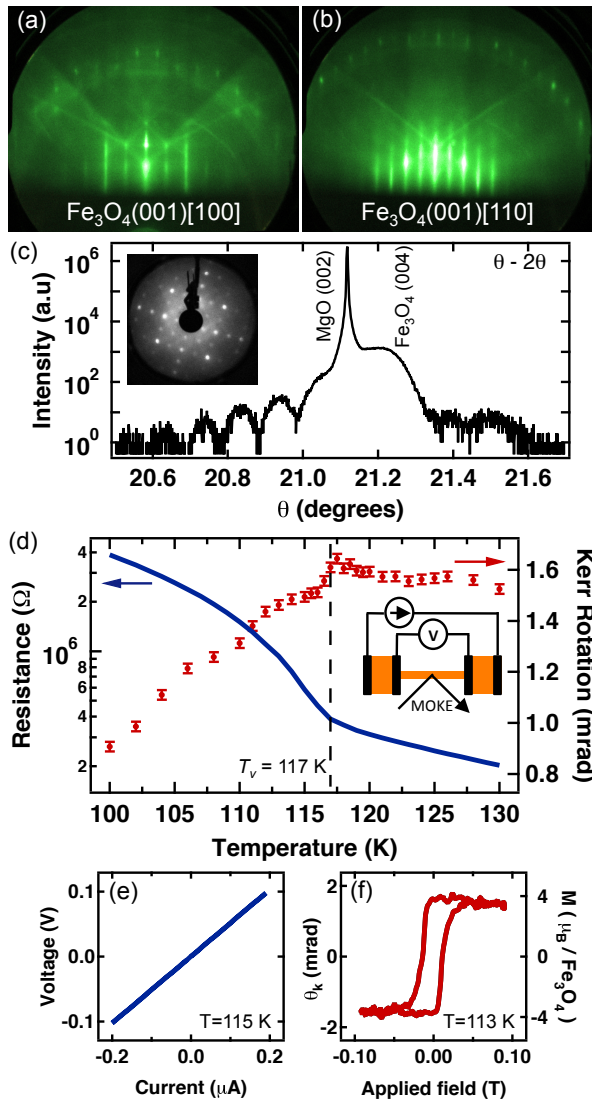


FIG. 1. Characterization of  $\text{Fe}_3\text{O}_4$  thin films. (a) and (b) are RHEED patterns for 50 nm  $\text{Fe}_3\text{O}_4$  on  $\text{MgO}(001)$  along the  $[100]$  and  $[110]$  in-plane directions, respectively. (c) HRXRD  $\theta - 2\theta$  scans measured around the location of the  $\text{MgO}(002)$  peak with Kiessig fringes. Inset: LEED pattern with incident energy of 160 eV. (d) Temperature dependence of resistance measured by four-point probe (blue) and magnetization measured by MOKE (red). The vertical dashed line indicates the Verwey transition. Inset: geometry for the resistance and magnetization measurements. (e)  $I$ - $V$  curve for  $\text{Fe}_3\text{O}_4$  channel at 115 K. (f) MOKE hysteresis loop for  $\text{Fe}_3\text{O}_4$  at 113 K. The right axis shows absolute magnetization based on SQUID measurements on corresponding samples.

perature, measurements are repeated to ensure the temperature is stable.

The magneto-optic Kerr effect (MOKE), with laser beam incident through the transparent  $\text{MgO}$  substrate, is used to characterize the magnetic properties of the  $\text{Fe}_3\text{O}_4$  films (812 nm wavelength,  $p$ -polarized,  $45^\circ$  angle of incidence). Figure 1f shows a typical longitudinal MOKE

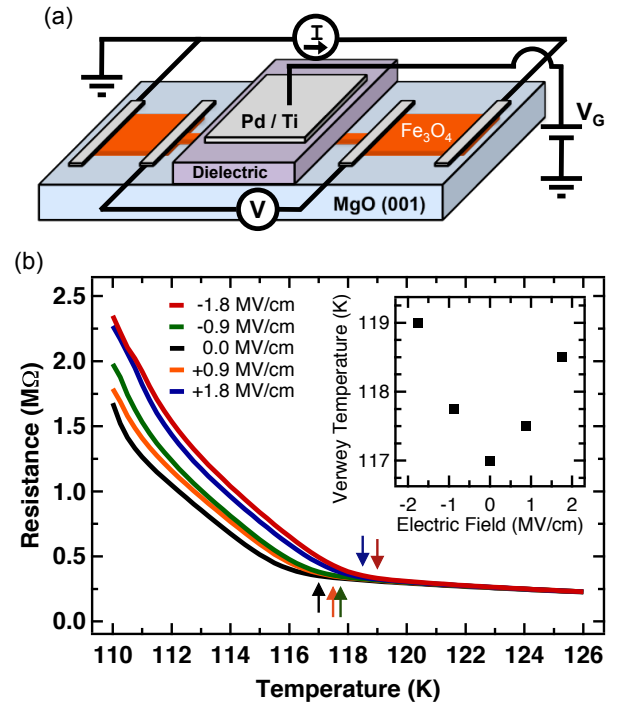


FIG. 2. Electrical gating of  $\text{Fe}_3\text{O}_4$  and manipulation of the Verwey transition. (a) A schematic of the sample device structure. The dielectric layer consists of PMMA(900 nm)/ $\text{Al}_2\text{O}_3$ (50 nm)/ $\text{MgO}$ (10 nm). Positive electric field corresponds to the application of positive voltage to the top gate electrode. (b) Temperature dependence of resistance for applied electric fields of +1.8 MV/cm (blue), +0.9 MV/cm (orange), 0.0 MV/cm (black), -0.9 MV/cm (green), -1.8 MV/cm (red). The arrows show  $T_V$  for each electric field, which is summarized in the inset.

hysteresis loop that exhibits large remanence and sharp magnetization reversal. The right hand axis of Fig. 1f displays the corresponding magnitude of the magnetization based on superconducting quantum interference device (SQUID) magnetometry. The temperature dependence of the MOKE signal (Figure 1d, red) exhibits a suppression of magnetization for temperatures below  $T_V$ . This behavior is characteristic of the Verwey transition.

To apply electric fields to the  $\text{Fe}_3\text{O}_4$  film, an insulating layer (PMMA/ $\text{Al}_2\text{O}_3$ / $\text{MgO}$ ) is deposited on top of the  $\text{Fe}_3\text{O}_4$ , followed by a metallic electrostatic gate (Pd/Ti), as shown schematically in Figure 2a. The devices are fabricated through several steps of evaporation using shadow masks. For the  $\text{Fe}_3\text{O}_4$  layer, a narrow channel is produced with a width of 210  $\mu\text{m}$ , creating a small active area to reduce the occurrence of pinholes and gate leakage. The  $\text{Fe}_3\text{O}_4$  channel length is 4.2 mm and the gate length is 3.3 mm. Alternate samples with  $\text{Fe}_3\text{O}_4$  films covering a large area of the substrate produce similar results [26]. Pd(100 nm)/Ti(15 nm) contacts (for four-point probe) are e-beam evaporated through a shadow mask in a separate system. Then a 10 nm  $\text{MgO}$  layer is grown on the

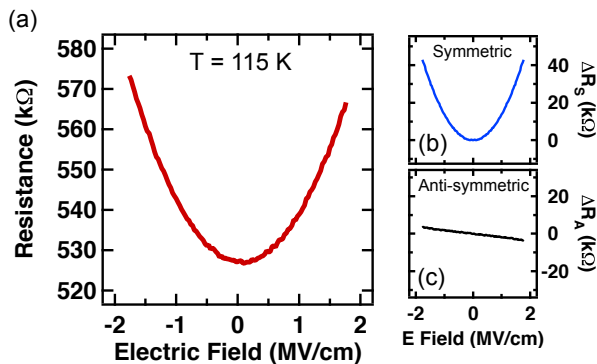


FIG. 3. Electrostatic gate dependence of resistance. (a) Gate dependent resistance for  $\text{Fe}_3\text{O}_4$  at a temperature of 115 K. (b) and (c) show the symmetric and anti-symmetric components of the gate dependent resistance change, respectively.

$\text{Fe}_3\text{O}_4$  followed by a 50 nm  $\text{Al}_2\text{O}_3$  layer. PMMA is then spin coated onto the sample at 3000 rpm and cured under a vacuum environment at  $170^\circ\text{C}$ . The spin coating and baking sequence is repeated three times giving a final PMMA layer thickness of 900 nm. Finally, a shadow mask is used to grow the Pd(100 nm)/Ti(15 nm) top gate electrode. Typical gate leakage is 0.5 nA for electric fields of  $\pm 1.8$  MV/cm.

An electric field is produced by applying a voltage ( $V_G$ ) between the gate electrode and the  $\text{Fe}_3\text{O}_4$  film. Figure 2b shows the temperature dependence of resistance for applied electric fields of +1.8 MV/cm ( $V_G = +60$  V, blue), +0.9 MV/cm ( $V_G = +30$  V, orange), 0 MV/cm ( $V_G = 0$  V black), -0.9 MV/cm ( $V_G = -30$  V, green), -1.8 MV/cm ( $V_G = -60$  V, red) with corresponding colored arrows indicating  $T_V$ . The data clearly show that  $T_V$  varies as a function of electric field, as summarized in the inset of Fig. 2c. At zero electric field,  $T_V$  is 117 K. Strikingly, both positive and negative electric fields cause  $T_V$  to increase, indicating that the shift in  $T_V$  depends primarily on the magnitude of electric field as opposed to its sign. The maximum effect is observed for -1.8 MV/cm, where  $T_V$  increases to 119 K, giving  $\Delta T_V = +2$  K. At a similar electric field, the largest  $\Delta T_V$  we observe in our study is  $\Delta T_V = +6$  K for a large area sample [26]. The increase of  $T_V$  cannot be due to Joule heating because a heating artifact would appear as a reduction of  $T_V$ . We also rule out effects of irreversible sample change by measuring the zero electric field temperature dependence of resistance before and after taking the data in Fig. 2b and no irreversible changes were observed. Finally, we observe that temperature dependent resistance above  $T_V$  does not change with applied electric field, which shows that the metallic phase is insensitive to electric field.

To gain further insight into the electric field effect, we perform a detailed study of the gate dependent resistance under isothermal conditions. Figure 3a shows the resistance at 115 K as the electric field is swept between +1.8

MV/cm and -1.8 MV/cm. Consistent with the shift in  $T_V$  (inset Fig. 2b), the resistance increases for both positive and negative electric fields and the effect is slightly larger for negative electric fields. To quantify the symmetry of the electric field effect, we separate the change in resistance  $\Delta R(E) = R(E) - R(0)$  into a symmetric part  $\Delta R_S(E) = [\Delta R(E) + \Delta R(-E)]/2$  (Fig. 3b) and anti-symmetric part  $\Delta R_A(E) = [\Delta R(E) - \Delta R(-E)]/2$  (Fig. 3c). Comparing Fig. 3b and 3c, the symmetric part is up to 11 times larger than the anti-symmetric part. Because the change in carrier concentration is proportional to  $E$  (i.e. anti-symmetric), the small contribution of  $\Delta R_A$  indicates that electric field control of the Verwey transition is not driven by a carrier concentration effect. Instead, a symmetric effect can be driven by other interactions with the electric field. The presence of an electric field will induce electric polarization given by  $P = \chi_e E = (\kappa - 1)\epsilon_0 E$ , where  $\chi_e$  is the electric susceptibility,  $\epsilon_0$  is the permittivity of free space, and  $\kappa$  is the relative dielectric constant of  $\text{Fe}_3\text{O}_4$ . The induced polarization will produce an energy contribution  $U = -\frac{1}{2}(PE) = -\frac{1}{2}(\kappa - 1)\epsilon_0 E^2$  that is symmetric in  $E$ . In addition, as  $\text{Fe}_3\text{O}_4$  undergoes the Verwey transition, the dielectric constant changes sharply with  $\kappa$  being larger for the insulating state than for the metallic state ( $\kappa_{ins} > \kappa_{metal}$ ) [27]. Thus, energy is lower for the insulating state than for the metallic state, which stabilizes the low temperature insulating state and causes  $T_V$  to increase. Therefore, this provides a macroscopic explanation for an electric field effect that is symmetric in  $E$  and produces an increase in  $T_V$ , consistent with experimental results. Further theoretical work is needed, including a microscopic model that can provide an explanation for the magnitude of the effect. In addition, a contribution from electric field induced strain could generate this symmetry and should also be investigated [18].

Since the Verwey transition in  $\text{Fe}_3\text{O}_4$  is a correlated phase transition that couples both the charge and magnetic properties, it should be possible to tune magnetic properties with applied electric field. Figure 4a shows MOKE hysteresis loops measured at 113 K with applied electric field of 0 MV/cm (black) and -1.8 MV/cm (red). The absolute magnetization is determined by SQUID measurements (right axis of Figure 4a). An electric field of -1.8 MV/cm causes a decrease in the saturation magnetization of 18%. Figure 4b displays the saturation magnetization as the electric field is swept between +1.8 MV/cm and -1.8 MV/cm. With the application of either positive or negative field, the magnetization decreases with a slightly stronger effect for negative fields. The magnetoelectric behavior is generated because the magnetization has strong temperature dependence below  $T_V$  (Figure 1d). When electric field is applied, the increase of  $T_V$  causes magnetization  $M$  to decrease because  $dM/dT$  is positive at  $T = 113$  K; the intuitive picture is that the  $M$  vs  $T$  curve of Fig. 1d shifts in temperature as  $T_V$

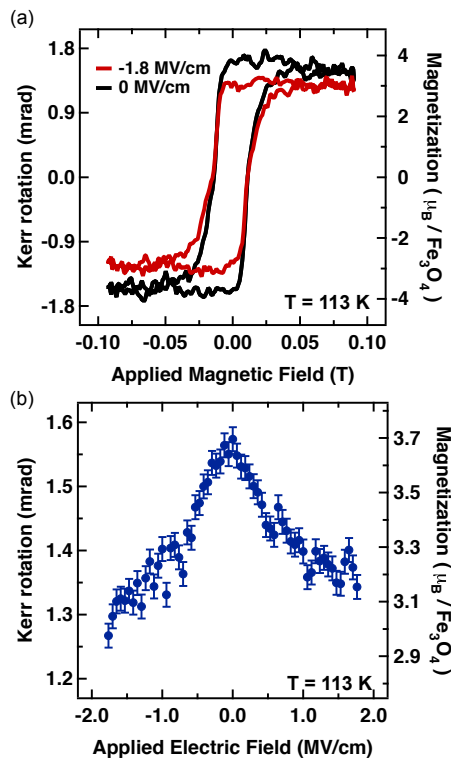


FIG. 4. Electrostatic gate dependence of magnetization. (a) MOKE loops measured at 113 K with applied electric fields of 0 MV/cm (black) and -1.8 MV/cm (red), showing a decrease in magnetization with the application of an electric field. (b) Magnetization as a function of electric field, demonstrating a magnetoelectric effect induced by electric field control of the Verwey transition.

increases. Thus, the decrease of magnetization for both positive and negative fields (with slightly stronger effect for negative fields) is consistent with the electric field dependence of  $T_V$  (Fig. 2b inset) and resistance (Fig. 3). The change in magnetization as a function of electric field is quantified by a magnetoelectric coefficient,  $\alpha_{ME} = |\Delta M/\Delta E|$ , where  $\Delta M$  is the change in magnetization and  $\Delta E$  is the change in electric field. Comparing the values at  $E = 0$  MV/cm and  $E = -1.8$  MV/cm yields a value of  $\alpha_{ME} = 585 \pm 39$  pT m/V. This is about an order of magnitude larger than in other single-phase magnetolectric materials, but not as large as some composite systems [26]. These results are compelling because they demonstrate a new method for generating magnetolectric effects by controlling a correlated phase transition.

In conclusion, we have demonstrated the electric field control of the Verwey transition in  $\text{Fe}_3\text{O}_4$  thin films. An electric field stabilizes the charge-ordered insulating state causing the Verwey transition temperature to increase. By manipulating a correlated phase transition that combines both charge and magnetic transitions, we realize a large and novel magnetolectric effect.

We acknowledge K. M. McCreary and P. M. Odenthal

for their assistance. This material is based on research sponsored by DARPA/Defense Microelectronics Activity (DMEA) under agreement number H94003-10-2-1004. We acknowledge Youli Li at the UCSB MRL Central Facilities (NSF Award No. DMR 1121053) for technical assistance with x-ray diffraction measurements and discussion.

\* roland.kawakami@ucr.edu

- [1] C. H. Ahn, Triscone, and J. M. Mannhart, *Nature* **424**, 1015 (2003).
- [2] A. Asamitsu, Y. Tomioka, H. Kuwahara, and Y. Tokura, *Nature* **388**, 50 (1997).
- [3] S. Lee, A. Fursina, J. T. Mayo, C. T. Yavuz, V. L. Colvin, R. G. S. Sofin, I. V. Shvets, and D. Natelson, *Nature Mater.* **7**, 130 (2008).
- [4] T. Lottermoser, T. Lonkai, U. Amann, D. Hohlwein, J. Ihringer, and M. Fiebig, *Nature* **430**, 541 (2004).
- [5] H. Zheng, J. Wang, S. E. Lofland, Z. Ma, L. Mohaddes-Ardabili, T. Zhao, L. Salamanca-Riba, S. R. Shinde, S. B. Ogale, F. Bai, D. Viehland, Y. Jia, D. G. Schlom, M. Wuttig, A. Roytburd, and R. Ramesh, *Science* **303**, 661 (2004).
- [6] E. J. W. Verwey, *Nature* **144**, 327 (1939).
- [7] E. J. W. Verwey and P. W. Haayman, *Physica* **8**, 979 (1941).
- [8] F. Walz, *J. Phys.: Condens. Matter* **14**, R285 (2002).
- [9] Y. Ding, D. Haskel, S. G. Ovchinnikov, Y.-C. Tseng, Y. S. Orlov, J. C. Lang, and H.-K. Mao, *Phys. Rev. Lett.* **100**, 045508 (2008).
- [10] J. Garcia, G. Subias, J. Herrero-Martin, J. Blasco, V. Cuartero, M. C. Sanchez, C. Mazzoli, and F. Yakhov, *Phys. Rev. Lett.* **102**, 176405 (2009).
- [11] D. J. Huang, H. J. Lin, J. Okamoto, K. S. Chao, H. T. Jeng, G. Y. Guo, C. H. Hsu, C. M. Huang, D. C. Ling, W. B. Wu, C. S. Yang, and C. T. Chen, *Phys. Rev. Lett.* **96**, 096401 (2006).
- [12] J. E. Lorenzo, C. Mazzoli, N. Jaouen, C. Detlefs, D. Manix, S. Grenier, Y. Joly, and C. Marin, *Phys. Rev. Lett.* **101**, 226401 (2008).
- [13] G. K. Rozenberg, M. P. Pasternak, W. M. Xu, Y. Amiel, M. Hanfland, M. Amboage, R. D. Taylor, and R. Jeanloz, *Phys. Rev. Lett.* **96**, 045705 (2006).
- [14] M. S. Senn, J. P. Wright, and J. P. Attfield, *Nature* **481**, 173 (2011).
- [15] F. Zhou and G. Ceder, *Phys. Rev. B* **81**, 205113 (2010).
- [16] J. H. Lee, L. Fang, E. Vlahos, X. Ke, Y. W. Jung, L. F. Kourkoutis, J.-W. Kim, P. J. Ryan, T. Heeg, M. Roedererath, V. Goian, M. Bernhagen, R. Uecker, P. C. Hammel, K. M. Rabe, S. Kamba, J. Schubert, J. W. Freeland, D. A. Muller, C. J. Fennie, P. Schiffer, V. Gopalan, E. Johnston-Halperin, and D. G. Schlom, *Nature* **466**, 954 (2010).
- [17] Y. Li, W. Han, A. G. Swartz, K. Pi, J. J. I. Wong, S. Mack, D. D. Awschalom, and R. K. Kawakami, *Phys. Rev. Lett.* **105**, 167203 (2010).
- [18] Y. Nagasawa, M. Kosaka, S. Katano, N. Mori, S. Tado, and Y. Uwatoko, *J. Phys. Soc. Jpn.* **76**, 110 (2007).
- [19] C. A. F. Vaz, J. Hoffman, A. B. Posadas, and C. H. Ahn,

- Appl. Phys. Lett. **94**, 022504 (2009).
- [20] F. Wang, C.-H. Li, T. Zou, L. Yi, and Y. Sun, J. Phys.: Condens. Matter **22**, 496001 (2010).
- [21] C. A. F. Vaz, J. Hoffman, Y. Segal, J. W. Reiner, R. D. Grober, Z. Zhang, C. H. Ahn, and F. J. Walker, Phys. Rev. Lett. **104**, 127202 (2010), pRL.
- [22] J. Ryu, A. V. Carazo, K. Uchino, and H.-E. Kim, Jpn. J. Appl. Phys. **40**, 4948 (2001).
- [23] J. Ryu, S. Priya, K. Uchino, and H.-E. Kim, J. Electroceram. **8**, 107 (2002).
- [24] L. Yan, Z. Wang, Z. Xing, and J. Li, J. Appl. Phys. **107**, 064106 (2010).
- [25] J. J. I. Wong, L. Ramirez, A. G. Swartz, A. Hoff, W. Han, Y. Li, and R. K. Kawakami, Phys. Rev. B **81**, 094406 (2010).
- [26] See Supplemental Material at <http://>.
- [27] A. Pimenov, S. Tachos, T. Rudolf, A. Loidl, D. Schrupp, M. Sing, R. Claessen, and V. A. M. Brabers, Phys. Rev. B **72**, 035131 (2005).